XFOIL: An Analysis and Design System for Low Reynolds Number Airfoils*

Mark Drela
MIT Dept. of Aeronautics and Astronautics, Cambridge, Massachusetts

Abstract

Calculation procedures for viscous/inviscid analysis and mixed-inverse design of subcritical airfoils are presented. An inviscid linear-vorticity panel method with a Karman-Tsien compressiblity correction is developed for direct and mixed-inverse modes. Source distributions superimposed on the airfoil and wake permit modeling of viscous layer influence on the potential flow. A two-equation lagged dissipation integral method is used to represent the viscous layers. Both laminar and turbulent layers are treated, with an e^9-type amplification formulation determinining the transition point. The boundary layer and transition equations are solved simultaneously with the inviscid flowfield by a global Newton method. The procedure is especially suitable for rapid analysis of low Reynolds number airfoil flows with transitional separation bubbles. Surface pressure distributions and entire polars are calculated and compared with experimental data. Design procedure examples are also presented.

1 Introduction

Effective airfoil design procedures require a fast and robust analysis method for on-design and off-design performance evaluation. Of the various airfoil analysis algorithms which have been developed to date, only the interacted viscous/inviscid zonal approaches have been fast and reliable enough for routine airfoil design work. For low Reynolds number airfoils ($Re < 1/2$ million), the demands on the analysis method become especially severe. Not only must the complex physics of transitional separation bubbles be captured, but the solution algorithm must be able to handle the very strong and nonlinear coupling between the viscous, transition, and inviscid formulations at a separation bubble.

Of the various calculation methods currently in use (GBK code [1] , GRUMFOIL code [2]), only the ISES code [3,4,5] can routinely predict low Reynolds number airfoil flowfields. Its fully compatible laminar and turbulent viscous formulations, a reliable transition formulation, and a global Newton solution method represent the necessary ingredients for prediction of such flows.

ISES has been successfully applied to the design of low Reynolds number airfoils for human-powered aircraft [6], analysis of established airfoils [7], and the design of high Reynolds number transonic transport airfoils, even though it can be demanding in terms of computer time. About two minutes are required to calculate an entire 20-point polar on a dedicated supercomputer. For users limited to a microVAX-class (0.1 MFLOP) machine, this may require several hours, which severely hinders the inherently iterative design process. A major goal in the development of the present XFOIL code was to significantly reduce these computational requirements while retaining the ability to predict low Reynolds number flows. The analysis formulation was also embedded in an interactive driver which also allows the designer to exercise inverse solver and a geometry-manipulation facility. The overall goal is to improve the productivity of the designer.

The present paper will outline the basic inviscid and viscous formulations of XFOIL, and demonstrate its performance on a number of airfoil cases. The mixed-inverse formulation and associated user interface will also be described. Finally, the code's overall design/analysis environment will be discussed.

* In: Low Reynolds Number Aerodynamics. Springer-Verlag Lec. Notes in Eng. 54. 1989.

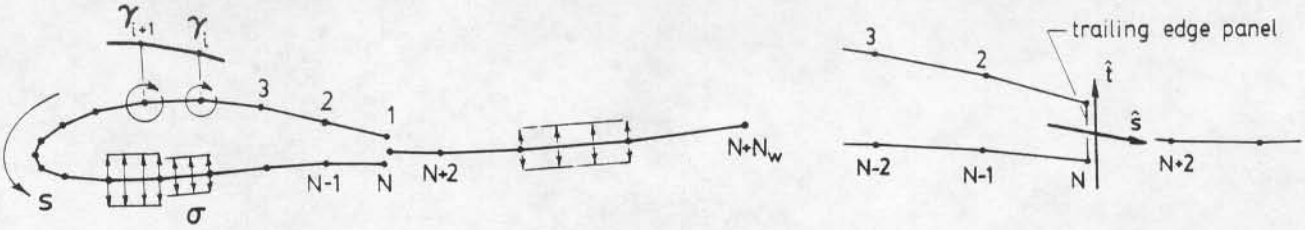

Figure 1: Airfoil and wake paneling with vorticity and source distributions, with trailing edge detail.

2 Inviscid Formulation

Numerous two-dimensional panel methods have been developed in the past [8,9,10], all being more or less successful for inviscid analysis of arbitrary airfoils. The present linear-vorticity streamfunction formulation is designed specifically for compatibility with an inverse mode, and for a natural incorporation of viscous displacement effects.

A general two-dimensional inviscid airfoil flowfield is constructed by the superposition of a freestream flow, a vortex sheet of strength γ on the airfoil surface, and a source sheet of strength σ on the airfoil surface and wake. The streamfunction of this configuration is given by

$$\Psi(x,y) \;=\; u_\infty y - v_\infty x + \frac{1}{2\pi}\int \gamma(s)\,\ln r(s;x,y)\,ds + \frac{1}{2\pi}\int \sigma(s)\,\theta(s;x,y)\,ds \qquad (1)$$

where s is the coordinate along the vortex and source sheets, r is the magnitude of the vector between the point at s and the field point x,y , θ is the vector's angle, and $u_\infty = q_\infty \cos\alpha$, $v_\infty = q_\infty \sin\alpha$ are the freestream velocity components.

The airfoil contour and wake trajectory are discretized into flat panels, with N panel nodes on the airfoil, and N_w nodes on the wake as shown in Figure 1. Each airfoil panel has a linear vorticity distribution defined by the node values γ_i $(1 \le i \le N)$. Each airfoil and wake panel also has a constant source strength σ_i $(1 \le i \le N+N_w-1)$ associated with it. These source strengths will be later related to viscous layer quantities.

A panel of uniform source strength σ_{TE} and vortex strength γ_{TE} must be also be placed across the airfoil trailing edge gap if it has a finite thickness. For smooth flow off the trailing edge, the trailing edge panel strengths σ_{TE} , γ_{TE} , must be related to the local airfoil surface vorticity by

$$\sigma_{TE} \;=\; \frac{1}{2}(\gamma_1 - \gamma_N)\,|\hat{s} \times \hat{t}| \qquad\qquad \gamma_{TE} \;=\; \frac{1}{2}(\gamma_1 - \gamma_N)\,|\hat{s} \cdot \hat{t}| \qquad (2)$$

where $\hat{s}$ is the unit vector bisecting the trailing edge angle, and $\hat{t}$ is the unit vector along the trailing edge panel as shown in Figure 1.

For the airfoil with flat panels, equation (1) evaluates to the following expression for the streamfunction at any field point x,y.

$$\begin{aligned}
\Psi(x,y) \;=\;& u_\infty y - v_\infty x + \frac{1}{4\pi}\sum_{j=1}^{N+N_w-1} \Psi_j^{\sigma}(x,y)\,2\sigma_j \\
&+ \frac{1}{4\pi}\sum_{j=1}^{N-1} \Psi_j^{\gamma+}(x,y)\,(\gamma_{j+1}+\gamma_j) \;+\; \Psi_j^{\gamma-}(x,y)\,(\gamma_{j+1}-\gamma_j) \\
&+ \frac{1}{4\pi}\left(\Psi_N^{\sigma}(x,y)\,|\hat{s}\times\hat{t}| \;+\; \Psi_N^{\gamma+}(x,y)\,|\hat{s}\cdot\hat{t}|\right)(\gamma_1-\gamma_N) \qquad (3)
\end{aligned}$$

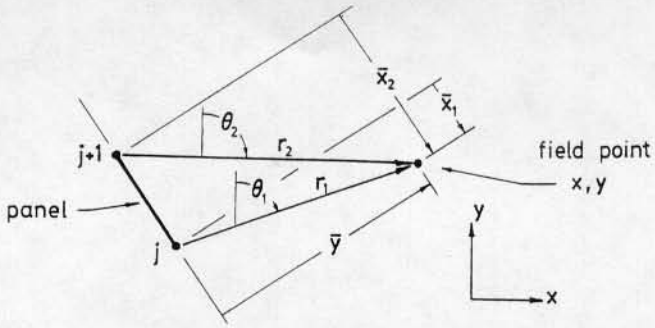

Figure 2: Local panel coordinates.

The unit streamfunctions in equation (3) are readily defined in terms of local panel coordinates $\bar{x} - \bar{y}$ as shown in Figure 2.

$$\Psi_j^{\gamma+}(x,y) = \bar{x}_1 \ln r_1 - \bar{x}_2 \ln r_2 + \bar{x}_2 - \bar{x}_1 + \bar{y}(\theta_1 - \theta_2) \tag{4}$$

$$\Psi_j^{\gamma-}(x,y) = \left[(\bar{x}_1 + \bar{x}_2)\Psi_j^{\gamma+} + r_2^2 \ln r_2 - r_1^2 \ln r_1 + \frac{1}{2}(\bar{x}_1^2 - \bar{x}_2^2) \right] \frac{1}{\bar{x}_1 - \bar{x}_2} \tag{5}$$

$$\Psi_j^{\sigma}(x,y) = \bar{x}_2\theta_2 - \bar{x}_1\theta_1 + \bar{y} \ln \frac{r_1}{r_2} \tag{6}$$

By requiring that the streamfunction be equal to some constant value Ψ_0 at each node on the airfoil, the following linear system results from the above relations.

$$\sum_{j=1}^{N} a_{ij}\,\gamma_j \; - \; \Psi_0 \; = \; -u_\infty y_i + v_\infty x_i \; - \sum_{j=1}^{N+N_w-1} b_{ij}\,\sigma_j \qquad ; \quad 1 \le i \le N \tag{7}$$

The coefficient matrices a_{ij} and b_{ij} are fully determined from the unit streamfunctions (4-6) if all the airfoil panel nodes x_i, y_i and the wake nodes are known. Combining the linear system (7) with a Kutta condition,

$$\gamma_1 + \gamma_N \; = \; 0 \tag{8}$$

gives a linear $(N{+}1) \times (N{+}1)$ system for the N node values γ_i and the airfoil surface streamfunction Ψ_0.

A special treatment is required for an airfoil with a sharp trailing edge. In this case the nodes $i = 1$ and $i = N$ coincide, and hence their corresponding equations in (7) are identical. The result is a singular system which cannot be solved for γ_i. To circumvent this problem, the $i = N$ equation in (7) is discarded and replaced by an extrapolation of the mean γ (between top and bottom) to the trailing edge.

$$(\gamma_3 - 2\gamma_2 + \gamma_1) \; - \; (\gamma_{N-2} - 2\gamma_{N-1} + \gamma_N) \; = \; 0 \tag{9}$$

2.1 Inviscid analysis procedure

For an analysis problem where the geometry is known, the linear system formed by the matrix equation (7) and Kutta condition (8) can be readily solved by Gaussian elimination. This gives the solution for the airfoil surface vorticity values as

$$\gamma_i \; = \; \gamma_{0_i} \cos\alpha \; + \; \gamma_{90_i} \sin\alpha \; + \sum_{j=1}^{N+N_w-1} b'_{ij}\,\sigma_j \qquad ; \quad 1 \le i \le N \tag{10}$$

where γ_0 and γ_{90} are the vorticity distributions corresponding to a freestream α of 0° and 90°, and $b'_{ij} = -a_{ij}^{-1} b_{ij}$ is the source-influence matrix. By setting $\sigma_i = 0$ in the surface vorticity expression (10) and specifying an angle of attack, an inviscid solution is immediately obtained. For viscous flows the source strengths σ_i are not known a priori, so the equation set (10) must be augmented with the boundary layer equations to obtain a solvable closed system. This will be dealt with in the viscous analysis section.

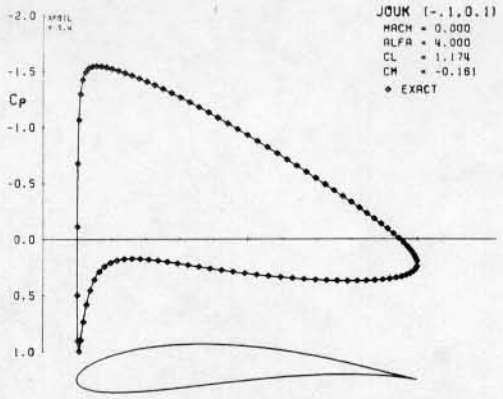

CPU Requirements on MicroVAX II

N	CPU (s)	C_L Error
40	4.0	0.766 %
60	7.5	0.340 %
100	20.0	0.175 %
160	54.0	0.085 %

Figure 3: Joukowsky airfoil test case. $N = 120$ C_P distribution shown.

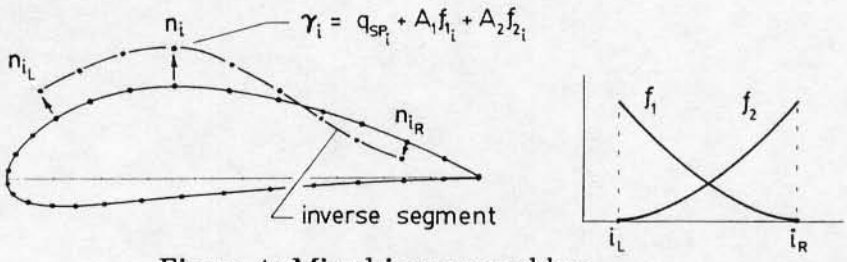

Figure 4: Mixed-inverse problem

Figure 3 shows the comparison between the calculated and exact pressure distributions on a Joukowsky airfoil. Since the flow inside the airfoil is stagnant, the surface velocity is equal to the surface vorticity, and hence the surface pressure coefficient is $C_p = 1 - (\gamma/q_\infty)^2$. Also shown is the accuracy and CPU requirements as functions of the number of panels. The results are typical of most panel methods.

2.2 Inviscid mixed-inverse procedure

A mixed-inverse problem results when the geometry is prescribed over a part of the airfoil surface, and the surface vorticity (or equivalently, speed), is prescribed over the remainder. The local unknown associated with any node i is then either the vorticity γ_i as in the analysis case, or the normal geometric displacement n_i of the node from a seed airfoil geometry as shown in Figure 4. The surface vorticity at node i is specified in the form

$$\gamma_i = q_{SPi} + A_1 f_{1i} + A_2 f_{2i} \tag{11}$$

which introduces two free parameters A_1 , A_2 into the specified vorticity distribution q_{SPi} . The free parameters weight the two specified shape functions f_{1i} , f_{2i} , which are specified to be quadratic over the inverse segment of the airfoil $i_R \leq i \leq i_L$. It is necessary to add the two degrees of freedom to the specified vorticity q_{SPi} in (11) to allow geometric continuity to be enforced at the two joining points between the inverse segment and the fixed part of the airfoil (Figure 4).

$$n_{i_L} = 0 \qquad\qquad n_{i_R} = 0 \tag{12}$$

This is consistent with the Lighthill constraints [10] which do not allow a totally arbitrary speed distribution on the airfoil. The inverse formulation of Kennedy and Marsden [9] does not address this issue, and hence cannot perfectly satisfy the necessary streamfunction constraint (7) at each panel node.

Since the governing streamfunction constraint (7) is nonlinear in the geometry, a Newton-Raphson procedure is used to solve the overall system. Eliminating the source distribution (only the inviscid inverse problem is treated), the equation system (7), the Kutta condition (8), and the geometry-continuity

conditions (12) are written as

$$\begin{aligned} \sum_{j=1}^{N} a_{ij}\,\gamma_j \;-\; \Psi_0 \;+\; u_\infty y_i - v_\infty x_i \;\equiv\; R_i \quad &= \; 0 \qquad ; \quad 1 \le i \le N \\ \gamma_1 + \gamma_N \;\equiv\; R_{N+1} \quad &= \; 0 \\ n_{i_L} \;\equiv\; R_{N+2} \quad &= \; 0 \\ n_{i_R} \;\equiv\; R_{N+3} \quad &= \; 0 \end{aligned} \tag{13}$$

and are then linearized about the current solution γ_i , x_i , y_i.

$$\begin{bmatrix} \\ \quad J_{ij} \quad \\ \\ \end{bmatrix} \begin{Bmatrix} \delta\gamma_j, \delta n_j \\ \delta\Psi_0 \\ \delta A_1 \\ \delta A_2 \end{Bmatrix} = \begin{Bmatrix} \\ -R_i \\ \\ \end{Bmatrix} \qquad ; \quad 1 \le i \le N+3 \tag{14}$$

The i,j entry of the Jacobian matrix J_{ij} is either $\partial R_i / \partial \gamma_j$ if the speed is unknown at node j, or $\partial R_i / \partial n_j$ if the node position is unknown at node j. To calculate the latter entry, the components n_x , n_y of the direction vector along which a node is to move are first locally specified, typically normal to the current airfoil surface. There follows

$$\frac{\partial R_i}{\partial n_j} \;=\; \frac{\partial R_i}{\partial x_j} n_x \;+\; \frac{\partial R_i}{\partial y_j} n_y \tag{15}$$

and the derivatives with respect to x_j and y_j are obtained in the formal manner from the definition of R_i (13). Ultimately this involves differentiating the unit streamfunction expressions (4 - 6), which is accomplished by a careful application of the chain rule.

The inverse solution proceeds by repeatedly solving the Newton system (14) for the variable changes and updating the current variables.

$$\Psi_0 \;\leftarrow\; \Psi_0 + \delta\Psi_0 \qquad A_1 \;\leftarrow\; A_1 + \delta A_1 \qquad A_2 \;\leftarrow\; A_2 + \delta A_2 \tag{16}$$

$$\gamma_i \;\leftarrow\; \gamma_i + \delta\gamma_i \qquad ; \quad i < i_R \;,\; i_L < i \tag{17}$$

$$x_i \;\leftarrow\; x_i + n_{x_i}\,\delta n_i \qquad ; \quad i_R \le i \le i_L \tag{18}$$

$$y_i \;\leftarrow\; y_i + n_{y_i}\,\delta n_i \qquad ; \quad i_R \le i \le i_L \tag{19}$$

$$\gamma_i \;\leftarrow\; q_{SPi} \;+\; A_1 f_{1i} \;+\; A_2 f_{2i} \qquad ; \quad i_R \le i \le i_L \tag{20}$$

Typically, two to four Newton iterations are required to converge to machine accuracy, depending on how much the airfoil geometry is to change. Assuming the same number of panels, each iteration requires approximately the same computational effort as that shown in Figure 3 for an inviscid analysis calculation.

The surface speed (or C_P) distribution for inverse calculations is specified as a function of the unwrapped fractional arc length on the as-yet-unknown airfoil. Figure 5 shows the old and specified distributions as viewed by the user, and the resulting calculated airfoil. The seed airfoil is a Wortmann FX63-137 airfoil at an angle of attack of 4°. The input speed distribution can be modified and the airfoil shape recalculated as often as needed.

A useful feature of the mixed-inverse formulation is that absolute control of geometry can be exersized where needed. Nevertheless, for preliminary design it is useful to employ a full-inverse algorithm which permits the speed distribution over the entire airfoil to be specified (subject to the Lighthill constraints). The XFOIL design environment includes such an algorithm, similar to the complex mapping method implemented by Eppler [10], to maximize the designer's flexibility. Prescribed surface speeds are input versus the surface arc length rather than the non-physical circle plane coordinate common to mapping methods. The distribution is input in the format shown in Figure 5, with the speed distribution of a seed airfoil being superimposed. The implementation also allows the trailing edge gap and trailing edge angle to be explicitly controlled.

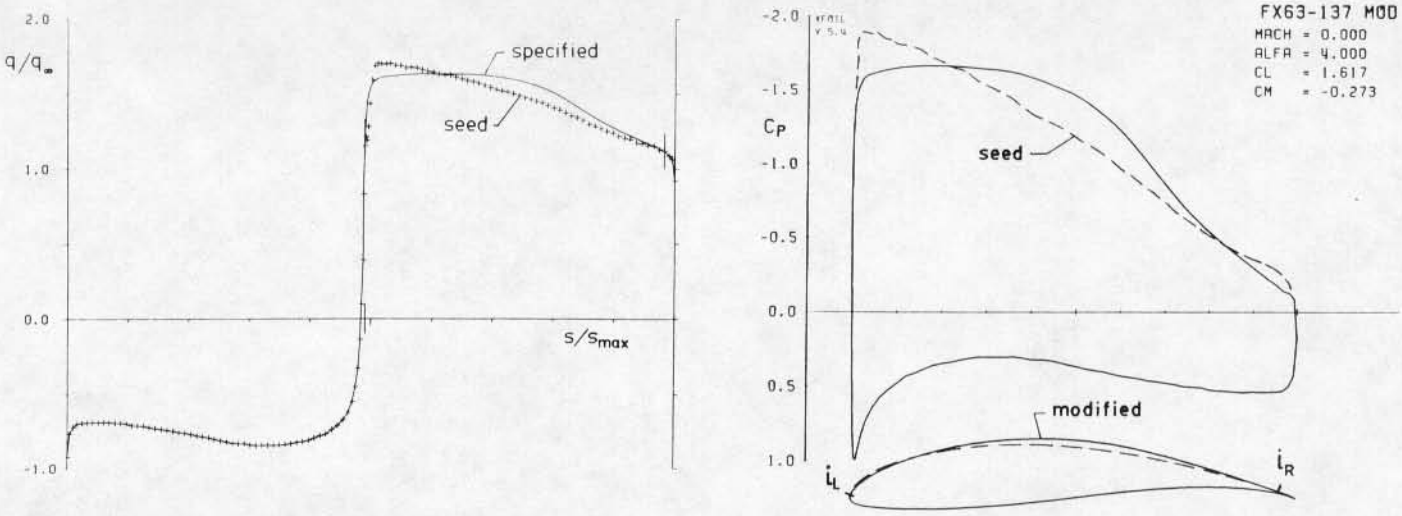

Figure 5: Input q_{sp} vs $s/s_{\max}$ (line) for local-inverse calculation, and calculated airfoil.

3 Viscous Formulation

The present viscous formulation of XFOIL is essentially the same as that of the transonic ISES code [5]. Some changes have been incorporated recently [11] to improve the prediction of "base drag" from blunt trailing edges. Only a summary description of the viscous formulation will be given, with more emphasis placed on the overall viscous/inviscid solution scheme which is unique to the present method.

3.1 Governing Equations and Closure

The viscous formulation employs the following standard compressible integral momentum and kinetic energy shape parameter equations. The streamwise coordinate is ξ.

$$\frac{d\theta}{d\xi} + (2 + H - M_e^2)\frac{\theta}{u_e}\frac{du_e}{d\xi} = \frac{C_f}{2} \tag{21}$$

$$\theta\frac{dH^*}{d\xi} + (2H^{**} + H^*(1-H))\frac{\theta}{u_e}\frac{du_e}{d\xi} = 2C_D - H^*\frac{C_f}{2} \tag{22}$$

Also, following Green et al [12], a rate equation for the maximum shear stress coefficient C_τ is used to account for deviations of the outer layer dissipation coefficient C_D from the local equilibrium value.

$$\frac{\delta}{C_\tau}\frac{dC_\tau}{d\xi} = 5.6\,(C_{\tau_{EQ}}^{1/2} - C_\tau^{1/2}) + 2\delta\left\{\frac{4}{3\delta^*}\left[\frac{C_f}{2} - \left(\frac{H_k - 1}{6.7H_k}\right)^2\right] - \frac{1}{u_e}\frac{du_e}{d\xi}\right\} \tag{23}$$

The latter equation has been altered slightly from the original formulation described in reference [5], and has resulted in better predictions of lift and drag near stall conditions.

In laminar regions, the shear stress lag equation (23) is replaced by a rate equation which models the growth of the amplitude $\tilde{n}$ of the most-amplified Tollmien-Schlichting wave.

$$\frac{d\tilde{n}}{d\xi} = \frac{d\tilde{n}}{dRe_\theta}(H_k)\,\frac{dRe_\theta}{d\xi}(H_k, \theta) \tag{24}$$

The empirical relation $d\tilde{n}/dRe_\theta\,(H_k)$ is a correlation of spatial growth rates computed from solutions to the Orr-Sommerfeld equation, and $dRe_\theta/d\xi\,(H_k, \theta)$ is obtained from the properties of the Falkner-Skan profile family. Reference [5] gives further details. The transition point is defined by the location where $\tilde{n}$ reaches a user-specified critical value $\tilde{n}_{\rm crit}$. This parameter in practice is used to represent the background

disturbance level and has quite a dramatic effect on low Reynolds number airfoil performance as will be shown in the results section.

The fundamental variables governed by the boundary layer equations are chosen to be θ, δ^*, and C_τ. In laminar regions, the amplification variable $\tilde{n}$ replaces C_τ. In addition, u_e is present as an external unknown which will be related to the global viscous solution via the inviscid outer flow. It is therefore only a convenient intermediate variable and does not constitute an additional unknown. To close the integral boundary layer equations (21), (22), and (23), auxilliary variables are defined in terms of θ, δ^*, C_τ, u_e or their suitable combinations with the following functional dependencies.

$$H_k = H_k(H, M_e) \qquad H^* = H^*(H_k, M_e, Re_\theta) \qquad H^{**} = H^{**}(H_k, M_e) \tag{25}$$

$$U_S = U_S(H^*, H, H_k) \qquad C_{\tau_{EQ}} = C_{\tau_{EQ}}(H^*, H, H_k, U_S) \qquad C_f = C_f(H_k, M_e, Re_\theta) \tag{26}$$

$$C_D = \frac{C_f}{2} U_S \; + \; C_\tau (1 - U_S) \tag{27}$$

The actual expressions for the above functional forms are given fully in references [5,11] and will not be repeated here.

The wake is treated as one viscous layer so that only one θ and one δ^* variable is present at each wake station, with the following initial conditions at the trailing edge.

$$\theta_{\text{wake}} \; = \; \theta_{\text{upper}} + \theta_{\text{lower}} \qquad \delta^*_{\text{wake}} \; = \; \delta^*_{\text{upper}} + \delta^*_{\text{lower}} + h_{TE} \tag{28}$$

This produces a continuous displacement body even with a blunt trailing edge of thickness h_{TE}. The initial wake shear coefficient is taken to be the θ-weighted average of the upper and lower surface values.

$$C_{\tau\,\text{wake}} = \frac{C_{\tau\,\text{upper}}\,\theta_{\text{upper}} + C_{\tau\,\text{lower}}\,\theta_{\text{lower}}}{\theta_{\text{upper}} + \theta_{\text{lower}}} \tag{29}$$

Additional minor corrections are incorporated for the blunt trailing edge case to better account for "base drag" as described in reference [11].

The governing equations (21-24) are discretized using two-point central differences (i.e. the trapezoidal rule). The boundary layer variables θ , δ^* , C_τ or $\tilde{n}$, and u_e are defined to be located at the panel nodes. Each airfoil and wake panel therefore has three coupled nonlinear equations associated with it which are solved by the procedure described below.

3.2 Viscous/Inviscid Coupling

Since the flow inside the airfoil is stagnant, on the airfoil surface u_e is simply equal to the local vorticity γ on the suction side, and $-\gamma$ on the pressure side. No such simple relation exists in the wake, and there it is necessary to relate u_e to the freestream and a sum of all the vorticity and sources on the airfoil,

$$u_{e_i} \; = \; \pm\gamma_i \qquad ; \quad 1 \le i \le N \tag{30}$$

$$\begin{aligned} u_{e_i} \; &= \; \nabla\Psi \cdot \hat{n} \\ &= \; u_\infty \hat{n}_y - v_\infty \hat{n}_x \; + \; \sum_{j=1}^{N} c^\gamma_{ij}\,\gamma_j \; + \; \sum_{j=1}^{N+N_w-1} c^\sigma_{ij}\,\sigma_j \qquad ; \quad N+1 \le i \le N+N_w \end{aligned} \tag{31}$$

with $\hat{n}$ being a unit vector locally normal to the wake. Evaluation of the source influence coefficients c^σ_{ij} in equation (31) requires modification of the assumed constant-source distribution on the wake panels, since this results in a logarithmic singularity in the velocity at each node. Using a two-piece linear source

distribution over each wake panel defined by using the neighboring panel source strengths eliminates this problem.

The influence of the viscous layer on the potential flow is properly modeled by the wall transpiration concept if the local source strength σ is equal to the local gradient of the mass defect $m \equiv u_e \delta^*$.

$$\sigma_i = \frac{dm}{d\xi} = \pm \frac{m_{i+1} - m_i}{s_{i+1} - s_i} \tag{32}$$

Substituting the general expression (10) for the surface vorticity γ into expressions (30,31), and eliminating the source strength σ in terms of the mass defect m as given by (32), produces the following.

$$u_{e_i} = u_{INV_i} + \sum_{j=1}^{N+N_w-1} d_{ij}\, m_j \qquad ; \qquad 1 \le i \le N+N_w \tag{33}$$

This very general expression gives the potential flow solution about the airfoil for any distribution of mass defect on the airfoil and wake. The "inviscid" edge velocity distribution u_{INV_i} and the mass-influence matrix d_{ij} are uniquely determined by the airfoil/wake geometry and freestream angle of attack, and are determined independently of the viscous solution (the wake node positions are determined by integrating an inviscid streamline trajectory from the trailing edge panel midpoint). It is important to note that d_{ij} embodies the effect of the local m_j near the trailing edge on the global u_{e_i} distribution via its effect on the Kutta condition. This "indirect" effect is quite significant for low Reynolds number flows, especially near stall or if a separation bubble occurs near the trailing edge. Previous expressions similar to (33) derived by Cebeci et al [13] for viscous/inviscid calculations require the repeated recalculation of the potential flow problem to determine this indirect effect. This represents a significant computational effort which is eliminated with the present formulation.

3.3 Newton solution

Since (33) is an explicit expression for u_{e_i} in terms of the boundary layer variables, it closes the discrete boundary layer equations (21-24). This nonlinear system, now rendered elliptic by the global mass influence on u_e, is solved by a full Newton method.

The Newton variables are defined to be $\delta\theta_i$, δm_i , and either $\delta\tilde{n}_i$ or $\delta C_{\tau i}$ depending on whether station i is laminar or turbulent. The Newton system thus has the following form.

$$\begin{bmatrix} & & \\ & J_{ij} & \\ & & \end{bmatrix} \begin{Bmatrix} \delta\theta_j \\ \delta m_j \\ \delta\tilde{n}_j\,,\ \delta C_{\tau j} \end{Bmatrix} = \begin{Bmatrix} \\ -R_i \\ \\ \end{Bmatrix} \qquad ; \quad 1 \le i \le N+N_w \tag{34}$$

The specific choice of δm instead of $\delta(\delta^*)$ as one of the Newton variables is made in the interest of efficiency, since in the former case only the δm_j columns in J_{ij} are full. The columns of the other variables $\delta\theta$, δC_τ , and $\delta\tilde{n}$ have entries only near the diagonal. Solving the Newton system (34) therefore requires only about 1/3 as much time as a full system of the same size. A custom solver is used to take full advantage of this feature.

3.4 Viscous Analysis Examples

Figure 6 shows computed polars for the Eppler 387 airfoil at three Reynolds numbers compared with measurements reported in reference [7]. Two calculated curves are shown for each Reynolds number, differing only in the specified disturbance parameter $\tilde{n}_{\text{crit}}$ described earlier. The curves corresponding

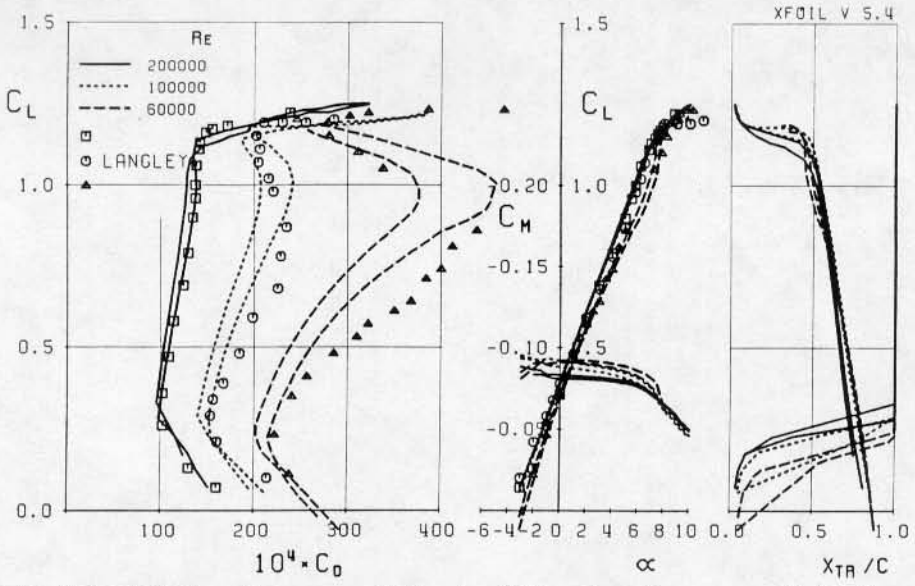

Figure 6: Calculated and measured Eppler 387 polars for $n_{\text{crit}} = 9, 12$ (lower, higher C_D).

to the lower disturbance levels have larger separation bubbles and show a higher drag, except near maximum lift where separation bubble loss has a relatively minor effect. This is consistent with the observed behavior of low Reynolds number airfoil flows. Overall the agreement is quite satisfactory, with accuracy degrading somewhat at the lowest Reynolds number.

Figure 7 shows computed and measured C_P distributions for one operating point and the MicroVAX II CPU time required. The dashed C_P curve is the "inviscid" u_{INV} distribution for that same α. As expected of a panel method, the CPU time is quite sensitive to panel density. For this case, the calculated result did not change significantly even for the smallest number of panels listed, indicating the method is quite fast. However, the number of panels appropriate for any given application depends primarily on the panel density required to resolve separation bubbles. A particularly severe test case in this regard is provided by an FX67-K-170 sailplane airfoil. At a Reynolds number of 2 million, this airfoil has small, but quite strong separation bubbles which must be resolved adequately for accurate drag prediction. Figure 8 shows the fractional error in C_L, C_D, C_m as a function of the number of panels on the entire airfoil. The "noise" in the error is due to panel nodes "moving" across the transition point as the number of panels is increased. For this case, $N = 120$ appears to be necessary to produce reasonably converged values. At lower Reynolds numbers where the bubbles are physically larger, and at higher Reynolds numbers where the bubbles contribute little to profile drag, the panel density requirements are lower. Local panel clustering in the vicinity of an anticipated bubble, which is readily specified with XFOIL's paneling routine, can also reduce panel number requirements and the associated computational effort.

4 Compressibility Correction

In the Karman-Tsien correction (derived in [14]), the compressible speed q and pressure coefficient C_P on an airfoil in compressible flow can be approximately determined from the incompressible flow values q_{inc} , $C_{P\text{inc}}$ by

$$C_P = \frac{C_{P\text{inc}}}{\beta + \lambda(1+\beta)\, C_{P\text{inc}}/2} \qquad q = \frac{q_{\text{inc}}\,(1-\lambda)}{1 - \lambda\,(q/q_\infty)^2_{\text{inc}}} \tag{35}$$

where $\beta = \sqrt{1 - M_\infty^2}$ and $\lambda = M_\infty^2/(1+\beta)^2$.

In the code implementation, all calculations are performed assuming the airfoil surface vorticity represents the incompressible speed q_{inc}. Relations (35) are used only to define the actual compressible

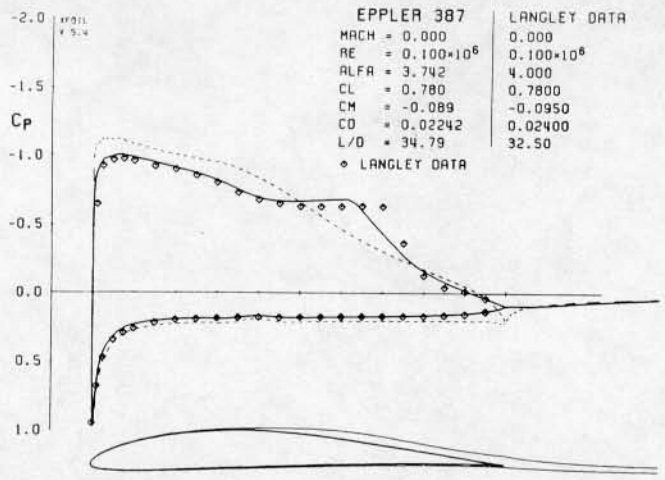

CPU Requirements on MicroVAX II

N	Startup CPU (s)	Newton it. CPU (s)	5 it. total CPU (s)
80	22.0	11.0	77.0
120	58.0	30.0	208.0
160	115.0	62.0	425.0

Figure 7: Calculated and measured C_P distributions and CPU requirements for Eppler 387 airfoil.

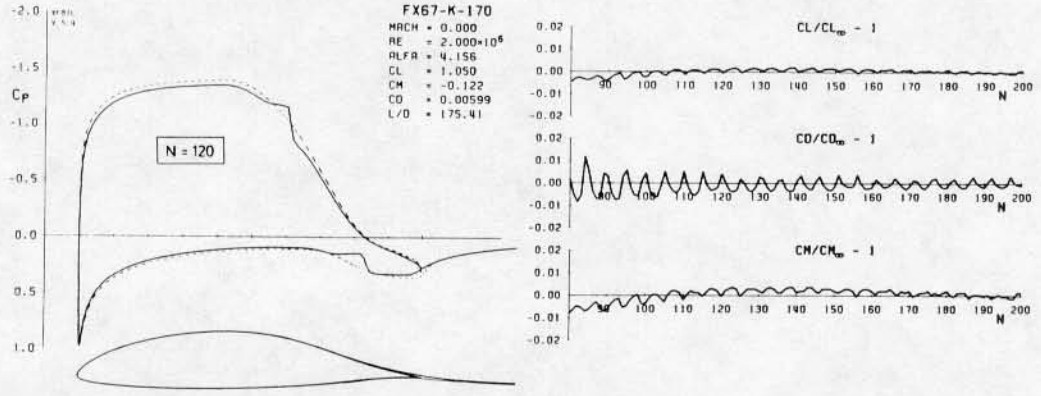

Figure 8: Error in C_L, C_D, C_m as a function of number of panels on an FX67-K-170 airfoil.

C_P for lift and moment calculations, and in conjunction with expression (33) to determine the actual compressible u_e seen by the boundary layer. The boundary layer formulation itself is already valid for compressible flows and requires no corrections.

Figure 9 shows a viscous calculation of a RAE 2822 airfoil compared with the experimental data of reference [15]. Reasonable agreement is obtained, despite the fact that the Karman-Tsien correction formally breaks down in supersonic flow. In practice, the method is reliable right up to sonic conditions, but rapidly degrades as significant supersonic regions appear. Hence, this correction extends the validity of XFOIL into the high-subsonic regime, and greatly extends its range of applicability.

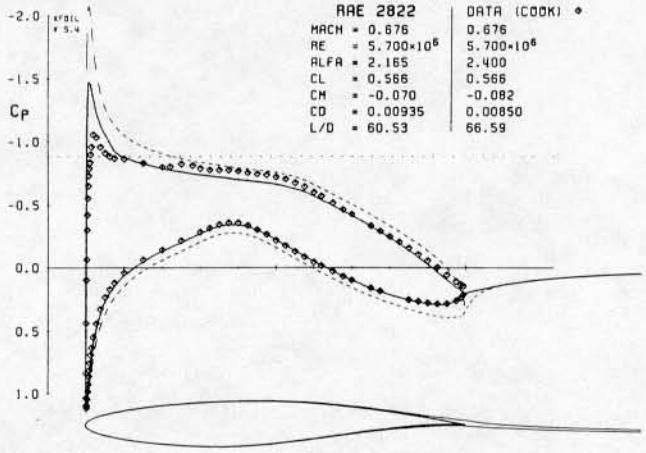

Figure 9: Calculated and experimental results for RAE 2822 airfoil near critical conditions.

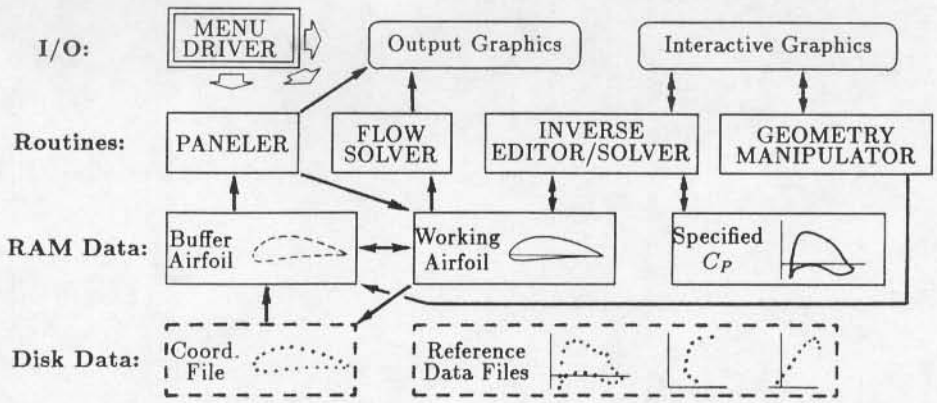

Figure 10: The XFOIL airfoil analysis/design system.

5 The XFOIL Design Environment

The overall XFOIL design/analysis system (Figure 10) consists of a collection of menu-driven routines which perform the viscous or inviscid analysis and inverse calculations. Supporting routines such as panel distribution generation, explicit geometry manipulation, disk I/O, and graphics are also driven from the same menu structure. The "Geometry Manipulator" allows explicit control of camber, thickness, leading edge radius, trailing edge gap, etc. This is very useful if inviolable geometric constraints must be met, and can be very effective for achieving certain aerodynamic specifications as well. For example, if a candidate airfoil's drag bucket is centered about $C_L = 0.5$, increasing its camber by a factor of 1.5 will center the bucket at approximately $C_L = 1.5 \times 0.5 = 0.75$. The Geometry Manipulator performs such a modification with one keyboard entry. Other capabilities include specifying flap deflections, changing camber via a specified loading change, and explicit contour input via a screen cursor.

Not shown in Figure 10 is a facility for calculating polars in batch mode, a convenience and a necessity if only modest computing power is available. The calculated polar points and associated surface pressure and boundary layer parameter distributions are saved in disk files and can be plotted later. The calculated polars shown in Figure 6 were generated in this manner.

6 Conclusions

The XFOIL airfoil design system outlined in this paper has proven to be a powerful and very useful tool for subcritical airfoil design, and is particularly applicable to low Reynolds number airfoils. Various graphics-oriented routines perform assorted analysis, inverse, and geometry-modification functions on a common airfoil representation, and can be easily exercised by the designer from a unified menu stucture with complete flexibility. Since all the important physical mechanisms which affect airfoil performance (instability, separation, bubble losses, etc.) are represented in the overall computational model, any airfoil modifications which are found to affect performance can be relied on to have a physical rather than numerical basis. The system thus allows the designer to quickly try out new design approaches and develop design philosophies for any given type of application.

Acknowledgements

This research was supported by the MIT Carl Richard Souderton Faculty Development Chair and the National Science Foundation Presidential Young Investigator Program.

References

[1] F. Bauer, P. Garabedian, D. Korn, and A. Jameson. Supercritical wing sections I, II, III. In *Lecture Notes in Economics and Mathematical Systems*, Springer-Verlag, New York, 1972, 1975, 1977.

[2] R. E. Melnik, R. R. Chow, and H. R. Mead. *Theory of Viscous Transonic Flow Over Airfoils at High Reynolds Number.* AIAA-77-680, Jun 1977.

[3] M. Drela and M. B. Giles. *ISES: A Two-Dimensional Viscous Aerodynamic Design and Analysis Code.* AIAA-87-0424, Jan 1987.

[4] M. B. Giles and M. Drela. Two-dimensional transonic aerodynamic design method. *AIAA Journal*, 25(9), Sep 1987.

[5] M. Drela and M. B. Giles. Viscous-inviscid analysis of transonic and low Reynolds number airfoils. *AIAA Journal*, 25(10), Oct 1987.

[6] M. Drela. Low-Reynolds number airfoil design for the MIT Daedalus prototype: A case study. *Journal of Aircraft*, 25(8), Aug 1988.

[7] R. J. McGhee, G. S. Jones, and R. Jouty. *Performance Characteristics from Wind-Tunnel Tests of a Low-Reynolds-Number Airfoil.* AIAA-88-6070, Jan 1988.

[8] E. Soinne and S Laine. An inverse boundary element method for single component airfoil design. *Journal of Aircraft*, 22(6):541–543, Jun 1985.

[9] J. L. Kennedy and D. J. Marsden. A potential flow design method for multicomponent airfoil sections. *Journal of Aircraft*, 15(1):47–52, Jan 1978.

[10] R. Eppler and D. M. Somers. *A Computer Program for the Design and Analysis of Low-Speed Airfoils.* NASA TM 80210, Aug 1980.

[11] M. Drela. *An Integral Boundary Layer Formulation for Blunt Trailing Edges.* AIAA-89-2200, Aug 1989.

[12] J. E. Green, D. J. Weeks, and J. W. F. Brooman. *Prediction of Turbulent Boundary Layers and Wakes in Compressible Flow by a Lag-Entrainment Method.* R & M Report 3791, Aeronautical Research Council, HMSO, London, 1977.

[13] T. Cebeci and R. W. Clark. An interactive approach to subsonic flows with separation. In *Second Symposium on Numerical and Physical Aspects of Aerodynamic Flows*, Long Beach, California, Jan 1983.

[14] A. H. Shapiro. *Compressible Fluid Flow I.* Wiley, New York, 1953.

[15] P. H. Cook, M. A. McDonald, and M. C. P. Firmin. Aerofoil RAE 2822 pressure distributions and boundary layer and wake measurements. In *Experimental Data Base for Computer Program Assessment, AR-138*, AGARD, 1979.